



*Supplement of*

## **Monitoring the impact of forest changes on carbon uptake with solar-induced fluorescence measurements from GOME-2A and TROPOMI for an Australian and Chinese case study**

**Juliëtte C. S. Anema et al.**

*Correspondence to:* Juliëtte C. S. Anema (juliette.anema@knmi.nl)

The copyright of individual parts of the supplement might differ from the article licence.

## S1 Trend correction GOME-2A SIF over northern China

To assess the stability of GOME-2A SIF (SIFTER v2) over north-central China, we used SIF time series over the nearby Gobi Desert (95.5–105.5° E, 40.5–44° N). Figure S1 shows the monthly GOME-2A SIF over the Gobi Desert from 2007 to 2018. The colors indicate the respective level-1 processor version over time. Over the early period, 2007–2013, a gradual trend

5 is noticed from around 2011. The striking positive shift in baseline SIF levels from July 2013 relates to the smaller range in viewing zenith angle (< 35°) following the swath reduction on 15 July 2013. From June 2014, the higher baseline trend appears to be broken for a period of 5–6 months. Figure S2 shows a similar structural break occurring over Sahara and 30–40°  
10 N ocean SIF pixels. The timing of the sudden drop in SIF signal coincides with the change of level-1 processor version 5.3 to 6.0 (18-05-2014) (Fig. S1), and thus suggests a significant influence of these changes on SIF. For our analysis, we solely use the GOME-2A data from the pre-2013 period to control the record's stability. Reprocessing the SIFTER v2 SIF data using level-1 data based on the recent processor version 6.3 that covers the entire data record will eliminate the uncertainty related to level-1 processor changes throughout the data record.

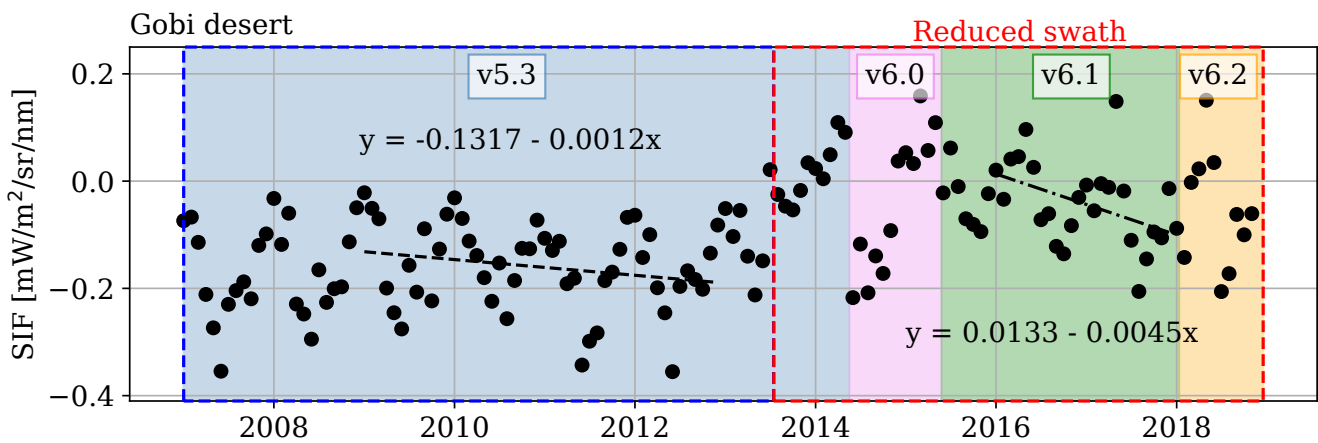


**Figure S1.** Monthly SIF retrieved from GOME-2A measurements as a function of time over the Gobi Desert (95.5–105.5 °E, 40.5–44 °N). The colored blocks indicate the used level-1 processor version (v5.3, v6.0, v6.1 and v6.2) over time. The record can be seen as coming from two different sensors, with the early and late period differentiated by timing of the swath reduction at 15-06-2013. The early period and late period are, respectively, indicated by the blue and red dotted blocks.

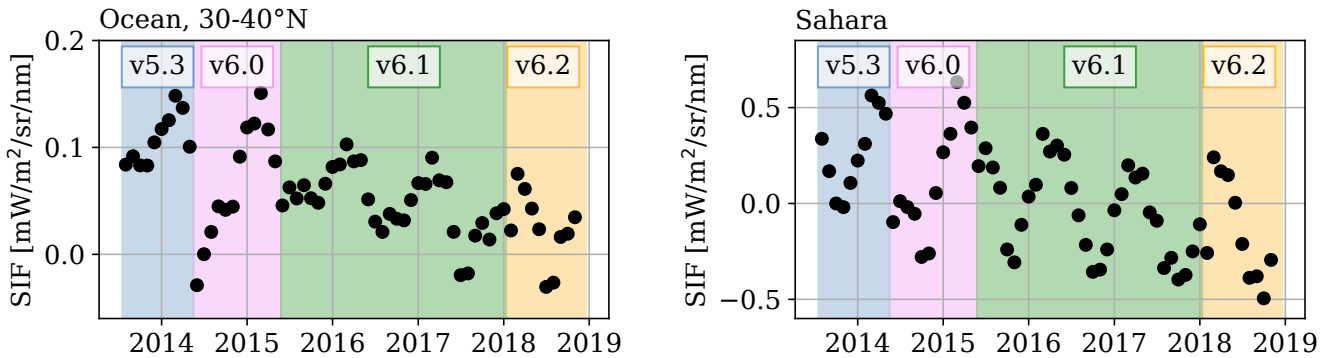


**Figure S2.** Monthly SIF retrieved from GOME-2A measurements as a function of time over the ocean (30 to 40° N) and the Sahara Desert (-8° W to 29° E, 15 to 30° N) over the late sensor period after the swath reduction at 15-06-2013. The colored blocks indicate the used level-1 processor version (v5.3, v6.0, v6.1 and v6.2) over time.

To correct for the noticed gradual trend over the early period, a multiplicative correction factor is applied. Gerlein-Safdi et al. (2020) used latitudinal average SIF to obtain multiplicative correction factors to correct for GOME-2A SIF over northern China (30–40° N). However, the SIF dynamics over the 30–40° N latitudinal band differ strongly over longitude: with higher SIF values over the west and lower over the east (e.g. north-central China). Furthermore, SIF cells that cover vegetational areas could represent the imprint of climatic variation and thus cause biases within the correction factor. The average of SIF over the Gobi desert (free of vegetation) area is expected to stay stable over time and not to be influenced by factors such as climatic fluctuation.

The year-specific correction factor is determined over the Gobi Desert area and corrects for the deviation in yearly SIF at year  $t$  with respect to the yearly SIF average over 2007 to 2012 the period of the reference spectra used in the SIFTER v2 retrieval. Therefore, the corrected SIF,  $F_{(C,i)}(t)$ , over cell  $i$  and year  $t$  is calculated as:

$$F_{C,i}(t) = F_i(t) \frac{\overline{F}_{\text{Gobi}}}{\overline{F}_{\text{Gobi}(07-12)}(t)} \quad (1)$$

where  $\overline{F}_{\text{Gobi}(07-12)}$  represents the 2007–2012 average of SIF over the Gobi Desert and  $\overline{F}_{\text{Gobi}}(t)$  the averaged SIF over the Gobi Desert in year  $t$ . Yearly SIF over the Gobi Desert is used to determine the correction to limit the uncertainty coming from the low signal levels over the area. Correction values deviate between 0.85 and 1.12. Figure S3 shows the correlation between FluxSat GPP with uncorrected and corrected GOME-2A SIF over our study region in China.

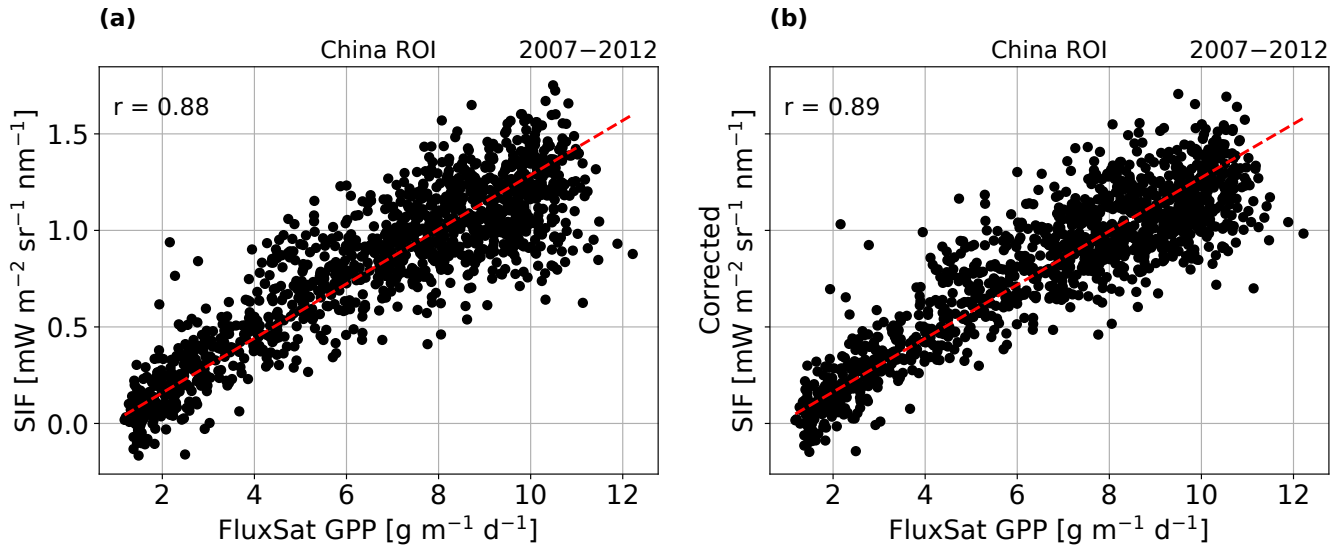


**Figure S3.** (a) Correlation between FluxSat GPP and SIF and (b) correlation between FluxSat GPP and corrected SIF over the China ROI area ( $104.5^{\circ}$ – $112^{\circ}$  E,  $31^{\circ}$ – $38^{\circ}$  N). The data points present SIF and GPP between 2007 and 2012 and over the summer period (June–August).

## S2 Relationships between TROPOMI SIF and GPP over Eucalyptus forest

The SIF–GPP relationship over Eucalyptus forest was obtained using TROPOMI SIF observations and GPP estimates from the eddy-covariance flux site in Tumbarumba (AU-TUM:  $35.66^{\circ}$  N,  $148.15^{\circ}$  E). We also used FluxSat GPP to infer an alternative SIF–GPP relationship over the Eucalyptus forest at Tumbarumba. To account for the smaller footprint of the eddy-covariance measurements, typically in the range of 100–1000 m, we selected TROPOMI SIF observations within a distance of 7 km of their center from the Tumbarumba site. The  $0.05^{\circ} \times 0.05^{\circ}$  FluxSat GPP cells, 8 in total, were selected to match the coverage of the selected TROPOMI SIF observations covering the flux tower.

SIF and the FluxSat GPP data have been co-sampled such that observations correspond to the same dates. The temporal co-sampling of SIF and GPP is of importance due to the (mostly) clear-sky bias of SIF observations from satellites, while GPP is measured under various conditions. Previous studies (e.g. Yang et al., 2015) shown different correlations between SIF and GPP under direct and diffuse light conditions. Therefore, it should be noted that the obtained relationship between SIF and GPP is specific for mostly clear-sky (direct light) conditions.

We inferred the empirical relationships from fitting instantaneous (TROPOMI overpass-time) SIF and daily-aggregated GPP data. In contrast to strategies using daily-corrected SIF for the analysis (Zhang et al., 2018; Turner et al., 2021), we chose here to use instantaneous SIF because the SIF signal in our region of interest is of low magnitude and the daily-correction would decrease the magnitude even further. Furthermore, the use of instantaneous SIF observations avoid simplified assumptions regarding the scaling of SIF with the amount of sunlight available for photosynthesis.

Reduced major axis regression (RMA) was used to obtain the empirical relationships between SIF and GPP. The RMA regression accounts for uncertainty in both the SIF observations and GPP data. The use of a linear regression is reasonable following the implied linear relation of SIF–GPP during most daily conditions (Porcar-Castell et al., 2014) as well as the enforced linearity due to integration of the over the canopy (Magney et al., 2020). The regression analysis of SIF vs GPP clearly indicates the presence an intercept for the best fit (Fig. S5). Furthermore, the top-of-canopy SIF depends on the escape ratio of the photons from the canopy and, theoretically, space-based SIF could approach to zero even if GPP is not 0.

**Table S1.** SIF–GPP relations using instantaneous TROPOMI SIF and daily GPP from the OzFlux dataset and FluxSat over the Tumbarumba flux tower. The OzFlux data represents the GPP estimates from the Tumbarumba tower. SIF is in units of  $\text{mW m}^{-2} \text{sr}^{-1} \text{nm}^{-1}$  and GPP in  $\text{gC m}^{-2} \text{day}^{-1}$ .

GPP source	SIF–GPP		SIF–GPP, no intercept
OzFlux	$r = 0.91$	$\text{GPP} = 11.10 \text{ SIF} + 0.81$	$\text{GPP} = 12.19 \text{ SIF}$
FluxSat	$r = 0.94$	$\text{GPP} = 5.56 \text{ SIF} + 1.37$	$\text{GPP} = 7.40 \text{ SIF}$

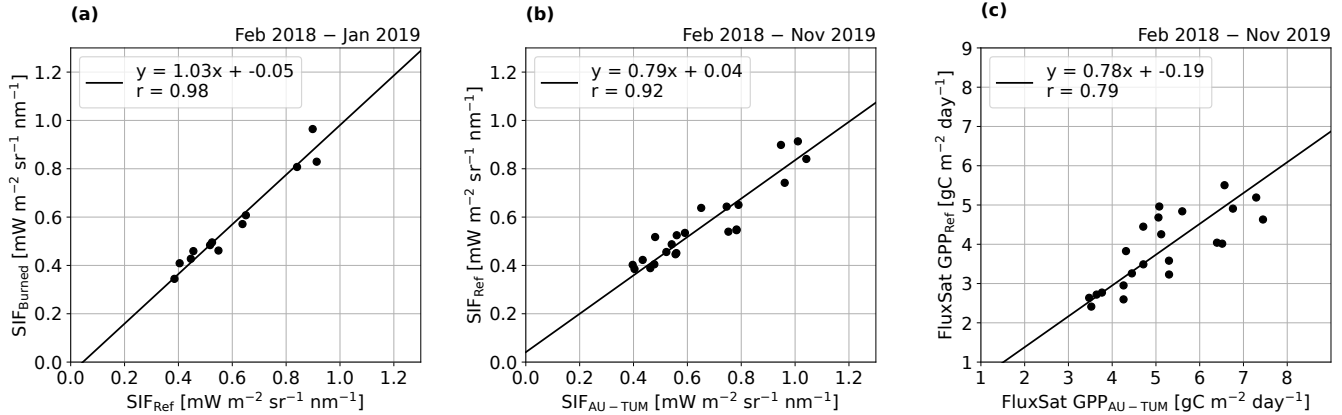


**Figure S4.** Correlation in the period February 2018 – January 2019 between (a) TROPOMI SIF over the reference area and area that would later burn down, and correlation in the period February 2018 – November 2019 between (b) TROPOMI SIF over the Tumbarumba flux tower site (AU-TUM) and TROPOMI SIF over the reference area. Subplot (c) shows the correlation between FluxSat GPP over the Tumbarumba site and the reference area.

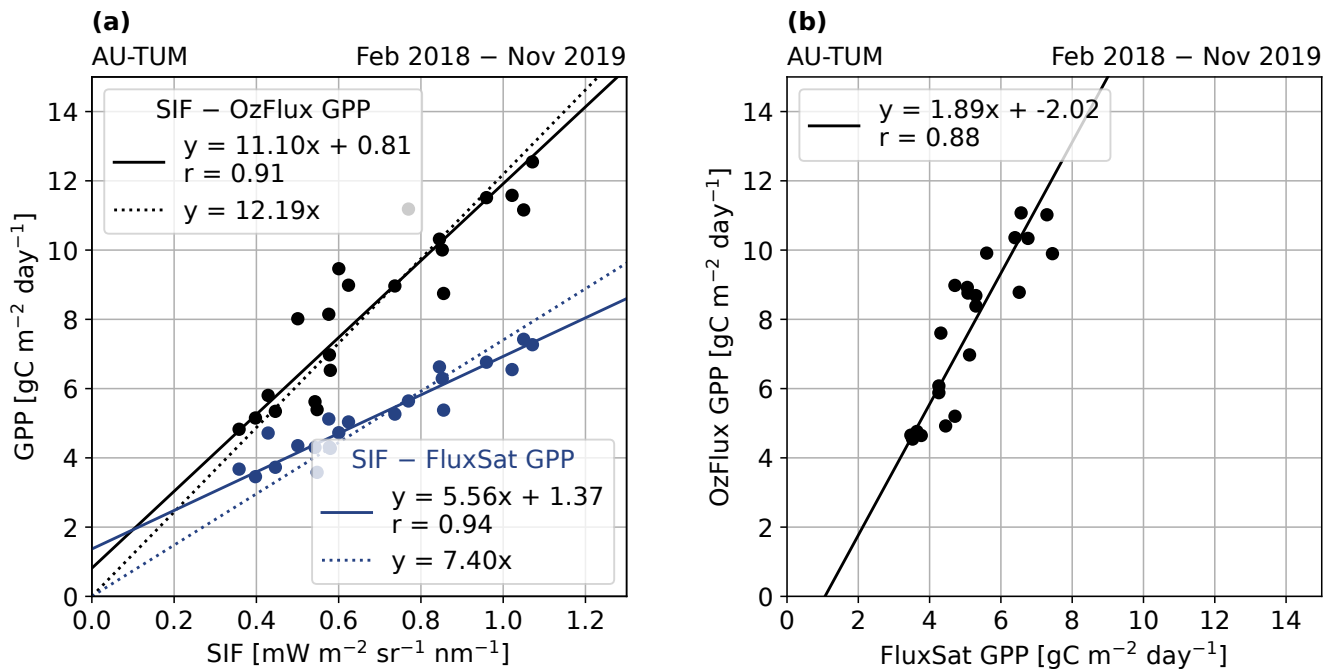


**Figure S5.** Correlation between (a) the TROPOMI SIF and daily GPP with flux tower and FluxSat GPP in black and blue, respectively, at the Tumbarumba Flux tower site (AU-TUM) and (b) monthly aggregated daily GPP versus the monthly averaged GPP where accounted days match SIF observations (collocated) at AU-TUM.

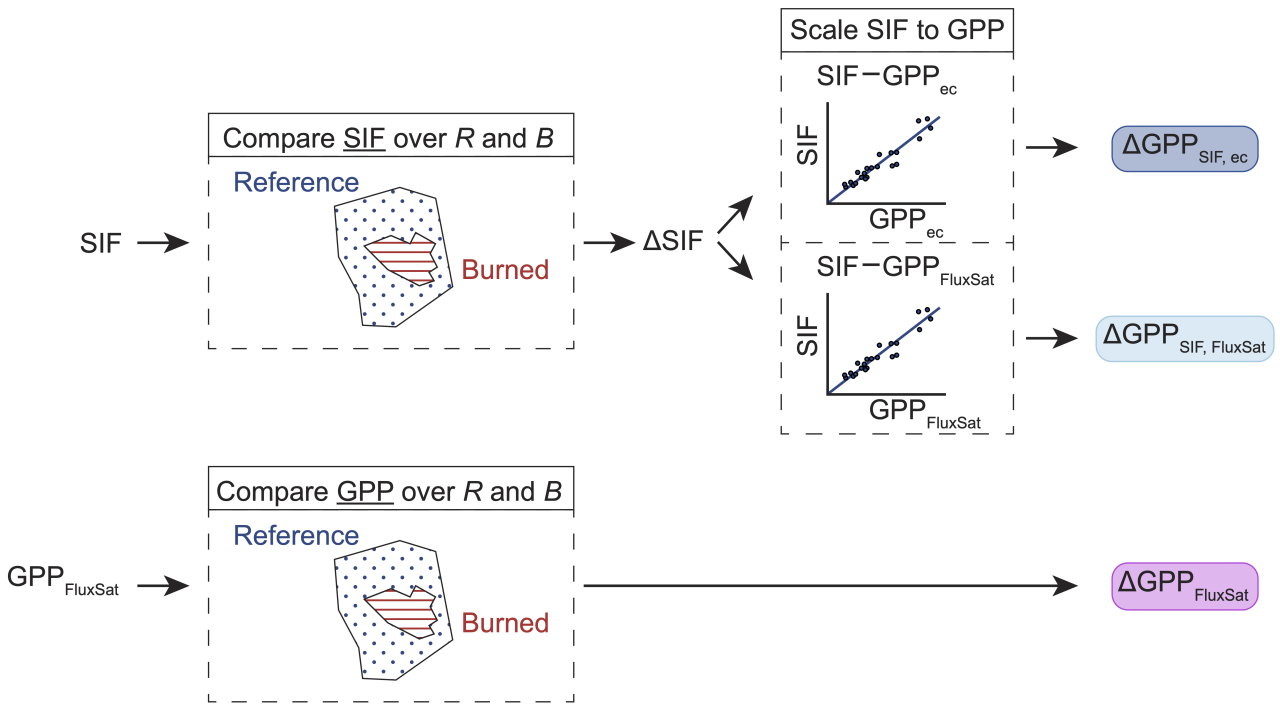


**Figure S6.** Outline of the derivation of the loss in GPP over the burned area: SIF-based GPPs, inferred from SIF–GPP relationship using eddy covariance data from the Tumbarumba OzFlux site and FluxSat GPP, and GPP directly from FluxSat GPP.

## S2.1 Uncertainty Analysis

We address uncertainties in the SIF-based estimated GPP loss via uncertainty propagation following equation ???. Factors considered include (1) SIF–GPP representativeness to Nunnett-Timbarra, (2) SIF–GPP representativeness to the post-fire period, and (3) detection of changes in TROPOMI SIF ( $\Delta$ SIF). For the  $\Delta$ GPP<sub>SIF, ec</sub> estimation, we address the uncertainty in (4) footprint differences between SIF observations and GPP estimates from the eddy-covariance flux tower.

55

1. Comparison of the ratio between FluxSat GPP and TROPOMI SIF obtained over the Tumbarumba tower and the Nunnett-Timbarra area show the similarity of both regions, namely  $7.44 \pm 1.00$  and  $7.72 \pm 1.25$  ( $\text{gC m}^{-2} \text{ day}^{-1}$ )/( $\text{mW m}^{-2} \text{ sr}^{-1} \text{ nm}^{-1}$ ). The ratios were computed from monthly SIF and GPP data over Feb. 2018 to Nov. 2019. The uncertainty within the SIF–GPP relationship itself is on the order of 10–15 %.
2. To assess the uncertainty in  $\Delta$ SIF detection, we examine monthly averaged TROPOMI SIF over the burned ( $B$ ) and reference ( $R$ ) area. Monthly averaged  $\text{SIF}_B$  and  $\text{SIF}_R$  are  $0.522$  and  $0.264 \text{ mW m}^{-2} \text{ sr}^{-1} \text{ nm}^{-1}$ , over Feb. 2019–Nov. 2019, respectively. Considering TROPOMI's single-measurement precision error of  $0.4 \text{ mW m}^{-2} \text{ sr}^{-1} \text{ nm}^{-1}$  (Köhler et al., 2018) and monthly pixel counts of  $185$  and  $32$  pixels over the reference and burned area, respectively, the error estimation is 30 %.
3. We compare the FluxSat GPP to TROPOMI SIF ratio over the burned area during Feb.–Nov. in 2018 (pre-fire) and 2019 (post-fire) to assess the uncertainty in applying the SIF–GPP relationship to post-fire conditions. The ratio was  $7.23 \pm 0.97$  ( $\text{gC m}^{-2} \text{ day}^{-1}$ )/( $\text{mW m}^{-2} \text{ sr}^{-1} \text{ nm}^{-1}$ ) for pre-fire and  $6.34 \pm 3.02$  ( $\text{gC m}^{-2} \text{ day}^{-1}$ )/( $\text{mW m}^{-2} \text{ sr}^{-1} \text{ nm}^{-1}$ ) for post-fire conditions, with the uncertainty in the post-fire ratio being approximately 50 %. Note that this analysis is limited due to the brief period between the Nunnett-Timbarra fire and a subsequent wildfire impacting the study area.

70 4. MODIS NDVI data (500 m resolution) indicates negligible uncertainty in footprint size differences, probably due to the  
extensive and uniform land cover around the Tumbarumba tower. Using MODIS pixels from 2009–2019 within (i) a 1  
km and (ii) a 9 km radius from the tower, representing the eddy covariance footprint size and selected TROPOMI SIF  
pixels/FluxSat GPP grid cells, NDVI values were  $0.77 \pm 0.05$  and  $0.77 \pm 0.04$ , respectively.

75 Adding these terms in quadrature, we estimate our estimates of SIF-based  $\Delta$ GPP are associated with a relative uncertainty  
of 60%.

### S3 Climate variability in Northern China

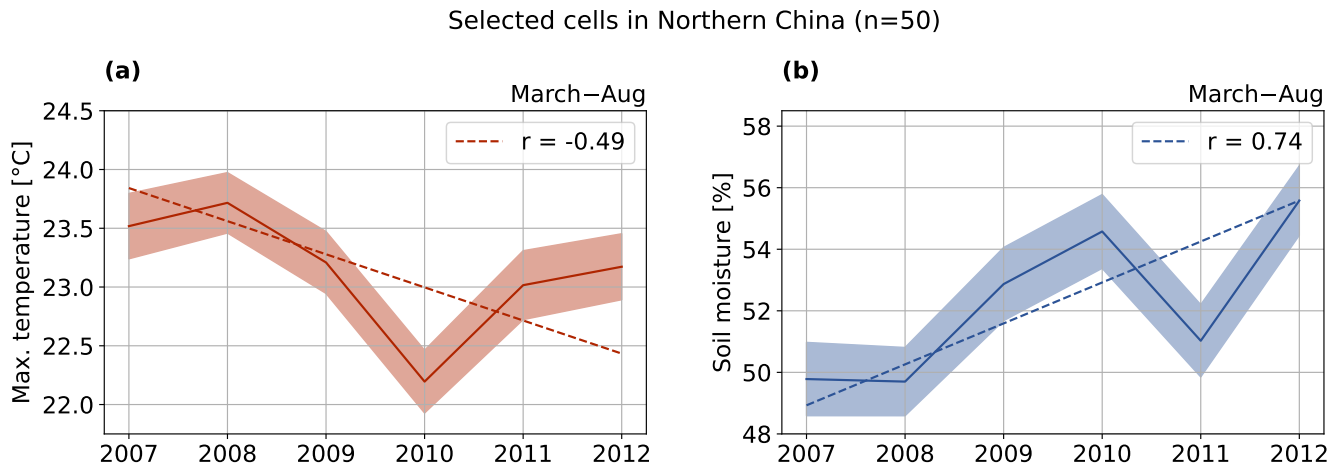


**Figure S7.** Temporal variability of climate variables (a) maximum temperature and (b) soil moisture, averaged over March–August and over all 50 selected (reforested and deforested) cells in the Northern China case study. The maximum temperature and soil moisture data are obtained from Muñoz Sabater (2019) and Dorigo et al. (2019), respectively, and were aggregated to a  $0.5^\circ \times 0.5^\circ$  grid.

## References

Dorigo, W., Preimesberger, W., Reimer, C., Van der Schalie, R., Pasik, A., De Jeu, R., and Paulik, C.: Soil moisture gridded data from 1978 to present, v201912.0.0., [https://cds.climate.copernicus.eu/cdsapp{#/dataset/satellite-soil-moisture?tab=overview}](https://cds.climate.copernicus.eu/cdsapp{#/dataset/satellite-soil-moisture?tab=overview), 2019.

80 Gerlein-Safdi, C., Keppel-Aleks, G., Wang, F., Frolking, S., and Mauzerall, D. L.: Satellite Monitoring of Natural Reforestation Efforts in China's Drylands, *One Earth*, 2, 98–108, <https://doi.org/10.1016/j.oneear.2019.12.015>, 2020.

Köhler, P., Frankenberg, C., Magney, T. S., Guanter, L., Joiner, J., and Landgraf, J.: Global Retrievals of Solar-Induced Chlorophyll Fluorescence With TROPOMI: First Results and Intersensor Comparison to OCO-2, *Geophysical Research Letters*, 45, 10,456–10,463, <https://doi.org/10.1029/2018GL079031>, 2018.

85 Magney, T. S., Barnes, M. L., and Yang, X.: On the Covariation of Chlorophyll Fluorescence and Photosynthesis Across Scales, *Geophysical Research Letters*, 47, 1–7, <https://doi.org/10.1029/2020GL091098>, 2020.

Muñoz Sabater, J.: ERA5-Land hourly data from 1981 to present, 10.24381/cds.e2161bac, 2019.

Porcar-Castell, A., Tyystjärvi, E., Atherton, J., Van Der Tol, C., Flexas, J., Pfundel, E. E., Moreno, J., Frankenberg, C., and Berry, J. A.: Linking chlorophyll a fluorescence to photosynthesis for remote sensing applications: Mechanisms and challenges, *Journal of Experimental Botany*, 65, 4065–4095, <https://doi.org/10.1093/jxb/eru191>, 2014.

Turner, A., Köhler, P., Magney, T., Frankenberg, C., Fung, I., and Cohen, R.: Extreme events driving year-to-year differences in gross primary productivity across the US, *Biogeosciences Discussions*, 1, 1–13, <https://doi.org/10.5194/bg-2021-49>, 2021.

90 Yang, X., Tang, J., Mustard, J. F., Lee, J. E., Rossini, M., Joiner, J., Munger, J. W., Kornfeld, A., and Richardson, A. D.: Solar-induced chlorophyll fluorescence that correlates with canopy photosynthesis on diurnal and seasonal scales in a temperate deciduous forest, *Geophysical Research Letters*, 42, 2977–2987, <https://doi.org/10.1002/2015GL063201>, 2015.

95 Zhang, Y., Xiao, X., Zhang, Y., Wolf, S., Zhou, S., Joiner, J., Guanter, L., Verma, M., Sun, Y., Yang, X., Paul-limoges, E., Gough, C. M., Wohlfahrt, G., Gioli, B., and Tol, C. V. D.: On the relationship between sub-daily instantaneous and daily total gross primary production : Implications for interpreting satellite-based SIF retrievals, *Remote Sensing of Environment*, 205, 276–289, <https://doi.org/10.1016/j.rse.2017.12.009>, 2018.